AGU PUBLICATIONS

Geophysical Research Letters

RESEARCH LETTER
10.1002/2015GL065336

Key Points:
- New method for source spectra estimates for shallow earthquakes
- New metrics for rupture dynamics analysis
- Nepal earthquake complex rupture propagation

Supporting Information:
- Supporting Information S1

Correspondence to:
M. A. Denolle,
mdenolle@ucsd.edu

Citation:
Denolle, M. A., W. Fan, and P. M. Shearer (2015), Dynamics of the 2015 *M*7.8 Nepal earthquake, *Geophys. Res. Lett.*, *42*, 7467–7475, doi:10.1002/2015GL065336.

Received 12 JUL 2015
Accepted 1 SEP 2015
Accepted article online 7 SEP 2015
Published online 25 SEP 2015

Dynamics of the 2015 *M*7.8 Nepal earthquake

Marine A. Denolle[1], Wenyuan Fan[1], and Peter M. Shearer[1]

[1]Scripps Institution of Oceanography, University of California, San Diego, La Jolla, California, USA

Abstract The 2015 *M*7.8 Nepal earthquake ruptured part of the Main Himalayan Thrust beneath Kathmandu. To study the dynamics of this event, we compute *P* wave spectra of the main shock and of two large aftershocks to estimate stress drop and radiated energy. We find that surface reflections (depth phases) of these shallow earthquakes produce interference that severely biases spectral measurements unless corrections are applied. Measures of earthquake dynamics for the main shock are within the range of estimates from global and regional earthquakes. We explore the azimuthal and temporal variations of radiated energy and highlight unique aspects of the *M*7.8 rupture. The beginning of the earthquake likely experienced a dynamic weakening mechanism immediately followed by an abrupt change in fault geometry. Correlation of backprojection results with frequency-dependent variations in the radiated energy rate and with the suggested geometry of the Main Himalayan Thrust yields new constraints on dynamic ruptures through geometrical barriers.

1. Introduction

The *M*7.8 Gorkha Earthquake of 25 April 2015 was highly destructive because of its low angle, shallow depth, and proximity to Nepal's capital, Kathmandu. The earthquake propagated along the Main Himalayan Thrust (MHT), between the Indian and the Eurasian plates, which accommodates a relatively fast shortening in Nepal of 20 mm/year [*Bilham et al.*, 1997; *Ader et al.*, 2012]. The Himalayan convergence is a unique case of continental subduction, and its background seismicity is atypical in that it does not illuminate the shallow-dipping locked part of the MHT [*Pandey et al.*, 1999]. In the along-dip direction, repeated topography profiles, GPS measurements, and the occurrence of concentrated seismicity provide a basis for constraining the geometry [*Cattin and Avouac*, 2000; *Lavé and Avouac*, 2001], in which crustal ramps at the base of a shallow-dipping detachment contribute to the uplift. Models of seismic coupling indicate that the MHT is fully locked up to the surface portion called the Main Frontal Thrust (MFT) [*Ader et al.*, 2012]. In the along-strike direction, spatial correlation of paleoseismic records provides constraints on past surface-rupturing megathrust earthquakes [*Jumar et al.*, 2006]. The Trisuli Transform [*Mugnier et al.*, 2011, Figure 1a] might be a natural barrier between the 1505 *M*8.2 rupture and the 1934 *M*8.1 and 1833 *M*8 earthquakes [*Bilham*, 1995; *Ambraseys and Douglas*, 2004] and coincides with a kink of seismicity [*Pandey et al.*, 1999, Figure 1a]. Geomorphology and thermal kinematic simulations suggest the presence of a lateral ramp and offsets in the location of the crustal ramp [*Berger et al.*, 2004; *Robert et al.*, 2011].

The 2015 *M*7.8 earthquake ruptured between the 1505 and the 1934 events. The Global Centroid-Moment-Tensor (GCMT) location and finite-fault slip inversions using long-period body waves (U.S. Geological Survey (USGS)), ScanSAR imaging [*Lindsey et al.*, 2015], and SAR interferometry (Geospatial Information Authority of Japan (GSI), [*Galetzka et al.*, 2015]) suggest that most of the slip occurred North of Kathmandu and East of the Trisuli Transform, whereas the epicenter is on the western edge of the slip distribution and of the Trisuli Transform (Figure 1a). Backprojection of teleseismic high-frequency *P* waves suggest a unilateral rupture to the east [*Avouac et al.*, 2015; *Yagi and Okuwaki*, 2015; *Fan and Shearer*, 2015], while low-frequency *P* waves suggest a rather complicated multistage rupture [*Fan and Shearer*, 2015], a result in general agreement with the GCMT solution and initial finite slip inversions (National Earthquake Information Center, USGS first solution). Long-period seismic and geodetic studies constrain the main areas of moment release and fault slip, but more detailed information on rupture dynamics requires observations of high-frequency body waves (0.1 Hz and above), which can be used to estimate corner frequencies and radiated energy. Here we combine teleseismic *P* wave spectral measurements with backprojection results that identity the locations of bursts of high-frequency energy, to produce a more complete view of the rupture dynamics of the *M*7.8 Nepal earthquake.

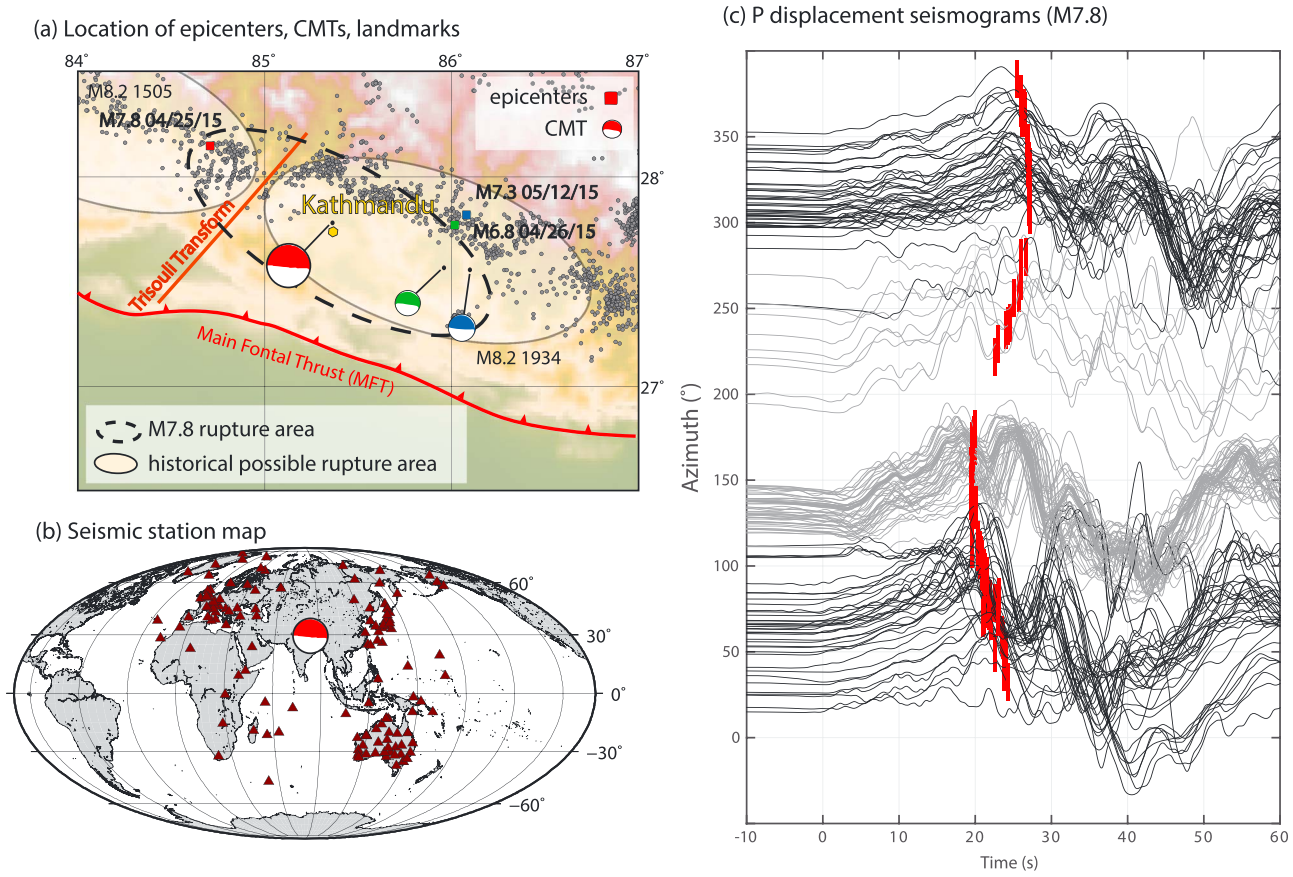

Figure 1. (a) Map of the area with landmarks, epicenters, and GCMT locations of the *M*7.8, *M*7.3, and *M*6.8 earthquakes, approximate historical rupture areas of the 1505 *M*8.2 and 1934 *M*8.1 earthquakes [*Ambraseys and Douglas*, 2004], and relocated seismicity [*Pandey et al.*, 1999; *Ader et al.*, 2012]. (b) Map of stations used in this study. (c) *M*7.8 main shock displacement *P* waveforms aligned to *P* arrival times recorded at Global Seismic Network stations with dark positive upward *P* motion and gray negative upward *P* motions; red markers denote the abrupt change in rupture dynamics.

2. *P* Wave Spectra, Stress Drop, and Radiated Energy

Records of *P* waves from shallow earthquakes (< 100 km) show the direct downgoing *P* wave immediately followed by the free-surface reflections (depth phases) *pP* and *sP*. The difference in arrival times between the depth phases and the direct phase depends on the source depth and on the *P* velocity to *S* velocity ratio above the source region. When the source pulses are separated enough that the phases can be clearly identified, the traveltime difference can be used to constrain earthquake depth [*Engdahl et al.*, 1998], but if the source pulses are wide enough that the phases overlap, the traveltime difference cannot be measured directly. However, even when the pulses overlap, the amplitude spectrum of the seismic wave train (*P*, *pP*, and *sP*) has a characteristic signature [e.g., *Warren and Shearer*, 2005] that provides a tool to constrain source depth. Depth phases also affect the low-frequency asymptote of the amplitude source spectrum [*Langston*, 1978] and, if ignored, strongly bias estimates of source spectral parameters such as corner frequency and seismic moment [*Hanks*, 1981; *Langston*, 1982]. This is illustrated in Figure 2a, which shows that ignoring the presence of depth phases in the spectra can produce overestimates of the true corner frequency and underestimates of the low-frequency asymptote. For most thrust mechanisms and for steep takeoff angles, the teleseismic *P* and *sP* phases arrive with opposite polarities, such that at shallow depths and for large earthquakes, they destructively interfere. Given a moment tensor to compute the radiation pattern, we can simultaneously constrain the source depth and the source amplitude spectrum by searching for the best fit to the *P* wave train spectra at individual stations.

We focus on the three largest events of the Nepal earthquake sequence, the *M*7.8 main shock of 25 April 2015, the *M*6.8 event of 26 April 2015, and the *M*7.3 event of 12 May 2015, which have good signal-to-noise over a broad frequency range. Two other large aftershocks were obscured by the surface waves of the *M*7.8 and

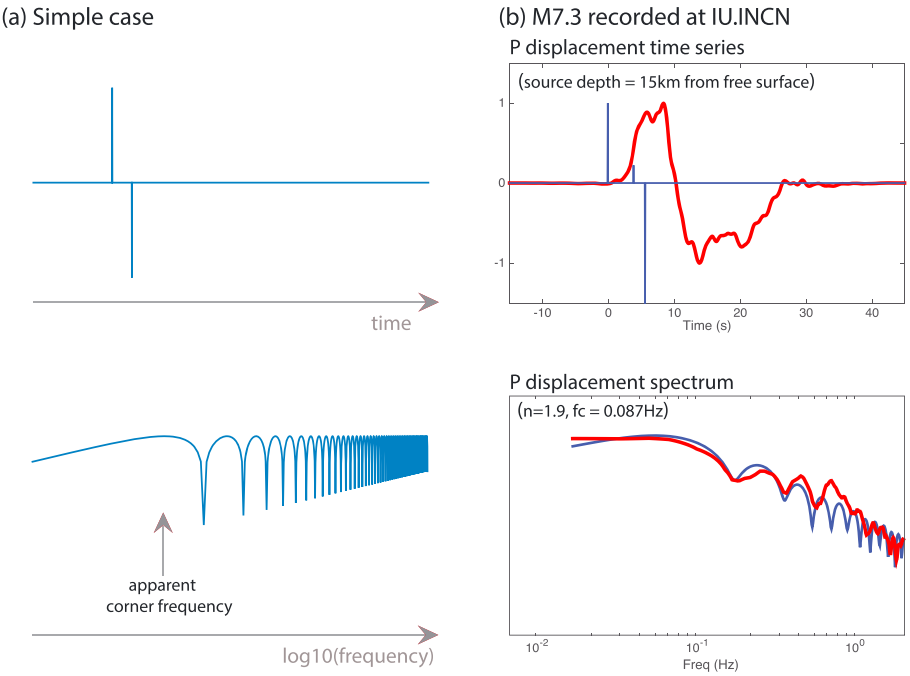

Figure 2. Illustration of depth phase effects. (a) Simplified case of two pulses with (Figure 2a, top) opposite polarity waveforms and (Figure 2a, bottom) their amplitude spectrum. (b) Observed *P* wave train from the *M*7.3 12 May 2015 shock (red), synthetic given the GCMT and the best fitting-depth from the free surface of 15 km (blue), and (Figure 2b, bottom) the amplitude spectra.

*M*7.3 events. We use vertical component records of the *P* waves from global and regional seismic networks (II, IU, MN, G, GE, AU, and JP) of stations within 30° and 90° of the earthquake epicenters (Figure 1c). We window the *P* wave train for 100 s for the *M*7.8 and 30 s for the *M*6.8 and *M*7.3 events, starting 15 s before the *P* arrival for both the main shock and aftershocks (see waveforms in Figure S1 in the supporting information). We apply a $\cos^2$ taper with tails of 15 s at the beginning and end of each time series.

At each station, we predict the amplitude spectrum of the *P* wave train in a homogeneous half space with shear wave speed $\beta = 3900$ m/s, density $\rho = 3000$ kg/m^3 in a Poisson medium ($\alpha = \sqrt{3}\beta$). We assume a Brune-type synthetic source spectrum, characterized by a corner frequency f_c, a high-frequency falloff rate n, and seismic moment M_0,

$$|\hat{S}(f)| = \frac{M_0}{1 + \left(f/f_c\right)^n}, \tag{1}$$

which we then convolve (multiply in the frequency domain) with the Green's function for the direct and depth phases. An example of this Green's function is shown by the stick seismograms in Figure 2b. Finally we correct the spectrum for attenuation by applying a $t^*(f)$ operator such that the corrected displacement spectra is given by $|\hat{S}(f)| = |\hat{u}(f)| \exp(\pi f t^*(f))$. We use the *Choy and Boatwright* [1995] model of t^*, also used in *Convers and Newman* [2011]:

$$\begin{aligned} t^*(f) &= 0.9 - 0.1\ \log_{10}(f), \quad f \le 0.1\text{Hz}, \\ t^*(f) &= 0.5 - 0.5\ \log_{10}(f), \quad 0.1\text{Hz} < f \le 1\text{Hz}, \\ t^*(f) &= 0.5 - 0.1\ \log_{10}(f), \quad f \ge 1\text{Hz}. \end{aligned} \tag{2}$$

We first estimate the source depth by best fitting the spectral shapes [*Warren and Shearer*, 2005]. The depths of the *M*6.8 and *M*7.3 aftershocks are well constrained as the misfit functions have a clear global minimum (Figure S3). However, it is difficult to find the minimum to the misfit function of the *M*7.8 main shock (see Figure S3c), likely due to the depth-varying geometry of the MHT so that we choose the GCMT depth (15 km) as focal depth. We find that the depth of the *M*6.8 is 18 km (compared to a GCMT depth of 17.4 km and a PDE depth of 24.8 km), which could be appropriate for the lower ramp [*Cattin and Avouac*, 2000] given the uncertainty in

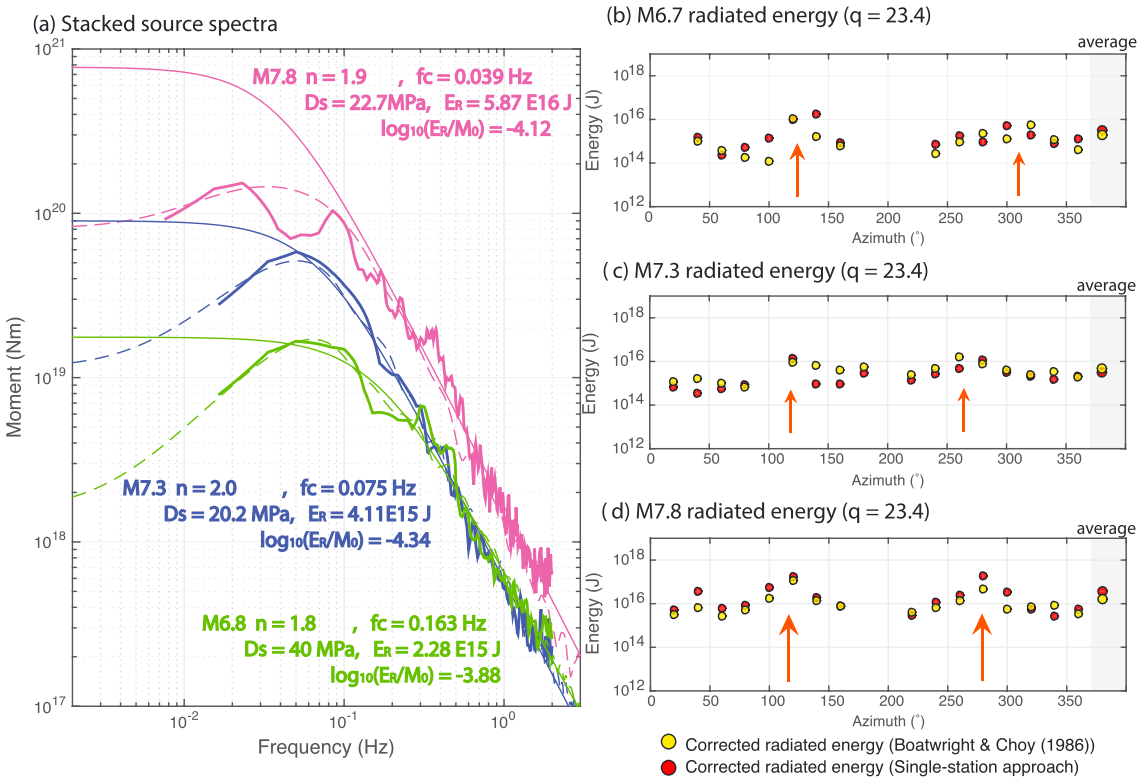

Figure 3. (a) Stacked *P* spectra (thick solid lines) and their best fitting source models (thin solid lines) and synthetic (thin dashed lines). Also listed are their high-frequency falloff rate *n*, corner frequency f_c, stress drop $\Delta\sigma$, total radiated energy E_R, and scaled radiated energy. (b–d) show radiated energy estimates from both the Boatwright and single-station methods as a function of azimuth for the *M*6.8, *M*7.3, and *M*7.8 events, respectively. Azimuths with relatively high radiated energy, suggesting possible directivity, are shown with the red arrows.

the MHT topography and locations of the hypocenter and GCMT, while the *M*7.3, which clearly has a different source time function (Figure S1) and is downdip of the *M*6.8, is shallower at 15 km (GCMT depth of 12 km and PDE depth of 15 km). The *M*7.3 is likely not on the plate interface but rather on a parallel fault, which has been proposed by structural studies [*Pandey et al.*, 1999; *Robinson et al.*, 2001; *Mugnier et al.*, 2013].

After constraining the source depths, we stack the observed spectra (Figure S2) and the depth-phase synthetic spectra over 20° azimuth bins to find the high-frequency falloff rates and the corner frequencies (Figures S6a–S6c) that best explain the observations of all three events and examine azimuthal variations in both parameters. Azimuthal variations in corner frequencies often reflect directivity effects, but variations in falloff rates have not yet been addressed in theoretical analyses and are thus harder to interpret. The overall stacks of the source spectra, performed over different azimuths, are shown in Figure 3a with the best fitting Brune-model predictions, both before (source model) and after including the effect of depth phases (i.e., convolving with the synthetic Green's function).

Corner frequency and moment can be used to estimate stress drop, but the result will depend upon which theoretical model is used for the calculation. Here we use the circular crack model of *Madariaga* [1976], in which stress drop $\Delta\sigma$ is given by

$$\Delta\sigma = M_0 \left(\frac{f_c}{0.42\beta} \right)^3 . \tag{3}$$

We use the Madariaga model not because it is necessarily the most accurate (see discussion in *Kaneko and Shearer* [2014, 2015]) but because it has been widely applied in other stress-drop studies [*Allmann and Shearer*, 2009; *Baltay et al.*, 2010; *Abercrombie*, 2014], making it easier to compare results. We use the model of a circular crack because deep penetration of the rupture shown in *Fan and Shearer* [2015]'s backprojection indicates an aspect ratio close to 1. To compute standard errors for corner frequency, $\log_{10}$ stress drop, and high-frequency falloff rate, we perform bootstrap resampling of the spectra that go into each azimuthal stack. We find that

the average stress drop (mean in log space) is 22.7 ± 1.9 MPa for the main shock, 20.2 ± 1.3 MPa for the *M*7.3, and 40 ± 1.5 MPa for the *M*6.8.

Because radiated energy contributes to the energy balance of earthquakes, high-frequency seismic waves carry a great deal of information on rupture dynamics. Radiated body wave energy is commonly calculated through two different approaches. *Boatwright* [1980] first developed a method to directly measure the radiated energy flux, which makes relatively few assumptions but which is sensitive to the geometrical spreading term and the radiation pattern and thus requires many receivers to average over the focal sphere.

The second method normalizes the zero-frequency asymptote of the amplitude spectrum to an independently derived seismic moment (e.g., the GCMT moment), thereby accounting for radiation pattern and geometrical spreading effects and assumes that the spectrum shape is well recovered at a single station. This method in principle provides the true total body wave energy from even a single station, presuming that its spectral shape is the same as that of the source spectrum (i.e., directivity or path effects have not distorted the spectrum) and that we have the correct moment. Because of this property, we refer to this as the single-station method, even though normally one would average the results from many stations. The single-station approach has been widely used in empirical Green's function studies [*Mayeda and Walter*, 1996; *Baltay et al.*, 2010, 2014]. Both methods require accurate knowledge of attenuation and of body wave velocities around the source.

The *P* wave Boatwright energy E_B and the single-station energy E_S integrate the source spectrum $\hat{S}(f)$,

$$E_S = \frac{2\pi M_0^2 \langle R_P^2 \rangle}{\rho \alpha^5} \int_0^\infty \left| f \widehat{\dot{S}}(f) \right|^2 \mathrm{d}f, \tag{4}$$

$$E_B = 32\pi^3 \mathcal{R}_P \rho \alpha \int_0^\infty \left| f \widehat{\dot{S}}(f) \right|^2 \mathrm{d}f, \tag{5}$$

where the operator $\dot{\cdot}$ denotes the amplitude normalization, ρ is density, α is *P* wave speed, M_0 is the seismic moment, $\langle R_P^2 \rangle = 4/15$ the squared radiation pattern of the *P* wave over the focal sphere, and $\mathcal{R}_P$ the geometrical spreading.

In real data, both approaches suffer from depth-phase interference and a limited frequency bandwidth. In our analysis, we build corrections for the biases using our synthetics in that we predict systematic errors in estimating energy from the limited frequency bandwidth synthetic spectra compared to the true energy known from the source spectrum. We then compute both energy estimates at all azimuth bins where we have high-quality stacked spectra. To obtain total radiated energy from *P* data alone, we assume that *S* and *P* share the same spectral shape such that their radiated energy ratio is $q = 23.4$. Figures 3b–3d show that both estimates (equations (4) and (5)) agree relatively well at all azimuths, compared to the uncorrected estimates (see Figure S5), and provide more details on the direction of high-frequency radiation. *Fan and Shearer* [2015] find the strongest overall directivity of the *M*7.8 main shock is at azimuth 130°. We find higher energy at this azimuth (see Figure 3d), consistent with directivity, but also see higher energy at an azimuth of 270°. Intriguingly, this suggests possible backward rupture in the direction normal to the crustal ramp, a result consistent with the suggestion from *Fan and Shearer* [2015] that there may be late-arriving energy from near the hypocenter. We find that the *M*6.8 aftershock is an energetic event, with large-scaled energy $\log_{10}(E_S/M_0) = -3.74$ compared to the other events, which results from its relatively high corner frequency and shallow high-frequency falloff rate. Remarkably, as shown in Figure 3, these differences mean that the *M*6.8 aftershock radiated as much energy as the *M*7.3 aftershock at frequencies above 0.3 Hz, despite its much lower moment. In contrast, the *M*7.3 aftershock has radiated energy, high-frequency falloff rate, and stress drop more typical of other earthquakes [e.g., *Baltay et al.*, 2014].

3. Rupture Dynamics of the *M*7.8 Main Shock

Waveform similarities between the onset of the main shock and its *M*6.8 aftershock are striking (Figures 1b, S1a, and S1b). Figure 4 shows that we can stretch the waveforms from the *M*6.8 to fit the duration and amplitude of the first 20–25 s of the *M*7.8 such that we respect self similarity (i.e., $M_0 \propto T^3$) between the large event displacement $U(t)$ and the small event displacement $u(t)$, $U(t) = b^2 u(bt)$. As shown in the example in Figure 4a, we find a stretching factor $b = 2.15$ that maximizes the correlation coefficient between the waveforms from

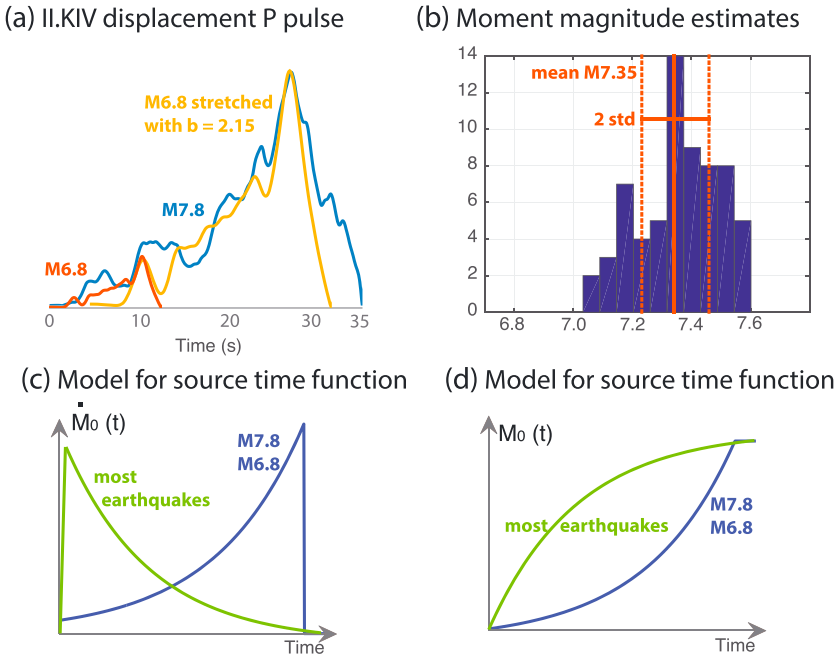

Figure 4. (a) *P* displacement seismograms (proportional to the moment rate function) of the main shock (blue), the *M*6.8 aftershock (red), and a stretched and scaled record of the aftershock at station II.KIV. (b) Histograms of the moment magnitudes estimated at each station and the average, given the mean of the best fit seismic moments. (c) Model for a *P* pulse that is proportional to the moment rate function $\dot{M}_0(t)$ with the function $\exp(t/T)$ compared to the function $\exp(-t/T)$, which most often describes slip rates in slip-weakening friction models. (d) Model for the slip function in both cases.

the *M*6.8 and the onset of the main shock. Performing similar analysis to all stations yields a seismic moment for the onset that corresponds to magnitude *M*7.3 ($\pm$ 0.14), which is only 20% of the total moment release. The *P* pulse exhibits slow growth that does not resemble typical slip-rate functions of self-similar cracks [*Kostrov*, 1974]. The first 20–25 s of the earthquake corresponds to the Stage 1 rupture described in *Fan and Shearer* [2015].

The similarity in the waveforms of the first 20–25 s of the *M*7.8 and the waveforms from the *M*6.8 likely reflects similar weakening mechanisms. Ductile behavior on the plate interface is expected to start at the foot of the crustal ramp [*Cattin and Avouac*, 2000; *Berger et al.*, 2004]. Proportional to the moment rate function, the shape of the *P* pulse suggests a slow initiation of slip and an acceleration phase with a power law time dependence, until the rupture either continues into the area of greatest moment release in the case of the *M*7.8 or stops in the case of the *M*6.8. This contrasts with most earthquake source time functions [*Houston*, 2001], which generally lack such a long and slow onset. Moreover, observations of nucleation phases [*Beroza and Ellsworth*, 1996] predict nucleation times on the order of 1 s for the equivalent earthquake sizes. Thus, dynamic weakening mechanisms likely produced the runaway rupture style of these two events. Such runaway behavior has been simulated in dynamic ruptures along a strong elastic mismatch at fault interfaces [*Shi and Ben-Zion*, 2006]. Other dynamic weakening mechanisms (trapped waves in the hanging wall that would feed the rupture propagation, flash heating, and thermal pressurization) should also be investigated, as dehydration and melting may occur as shallow as 35 km on the MHT [*Lemonnier et al.*, 1999], and seismicity has been correlated with rain fall due to the monsoons [*Bollinger et al.*, 2007].

An abrupt transition in the main shock rupture occurs between 20 and 25 s. To study this sudden change, we cut each seismogram into 10 s windows, overlapping by 0.5 s, and construct source spectra by removing path effects (equation (2)). For each window, we analyze the high-frequency radiation by (i) measuring the high-frequency falloff rate, (ii) estimating the radiated energy rate using equation (5) (corrected for the depth-phase bias), and (iii) computing the ratio of radiated energy within the bands 0.2 Hz–0.5 Hz and 0.5 Hz–2 Hz to the total estimated radiated energy rate.

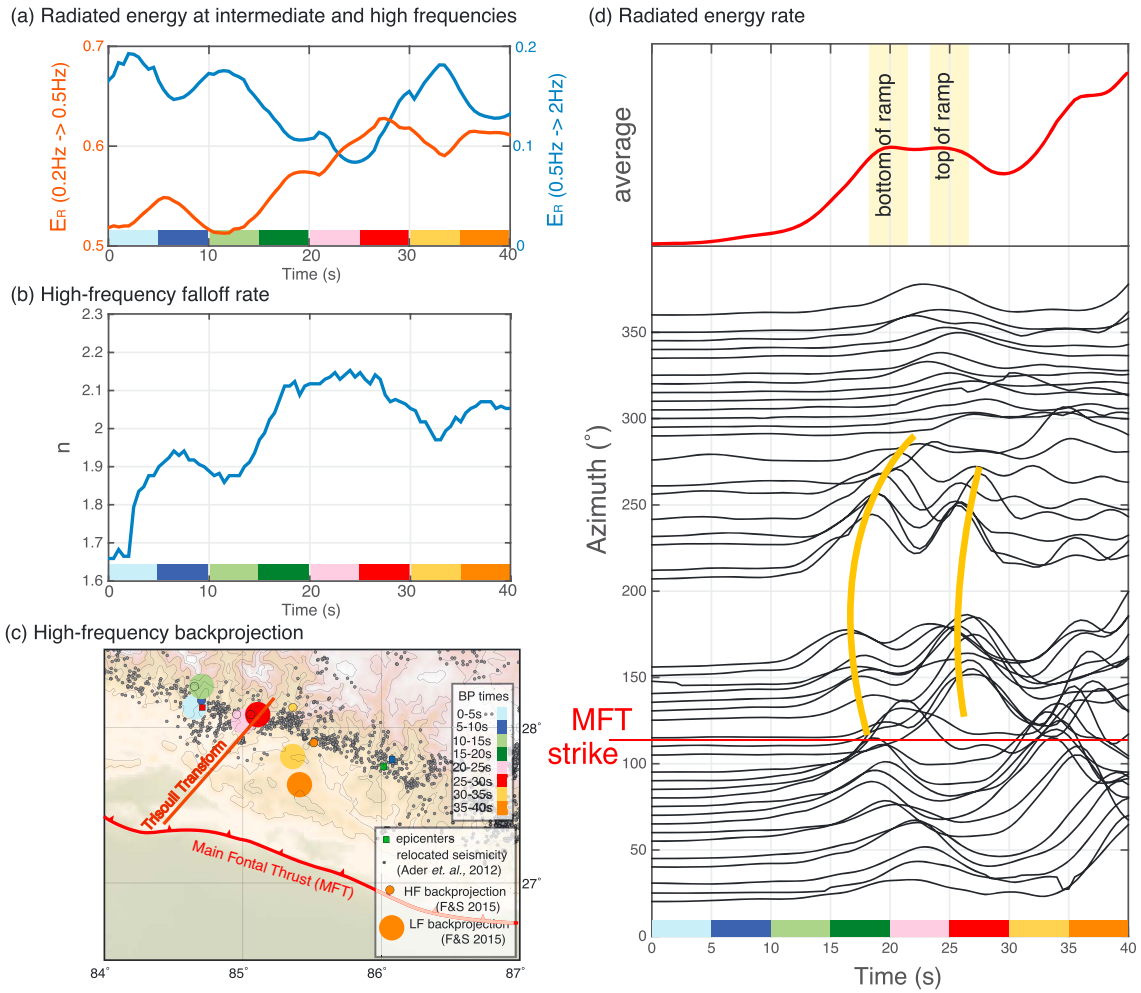

Figure 5. High-frequency radiation throughout the main shock rupture from spectrogram analysis. (a) Proportion of intermediate- and high-frequency (0.2 Hz–0.5 Hz and 0.5 Hz–2 Hz) energy and (b) high-frequency falloff rates within 10 s running time windows. (c) Spatial and temporal location of the low- and high-frequency energy from backprojection [*Fan and Shearer*, 2015]. (d) Measure of radiated energy with time versus azimuth (black, bottom) and the azimuthal average (red, top). The yellow highlights show times when the rupture propagates through the ramp.

Figures 5a and 5b show that the slow onset is enriched in high frequencies, with high-frequency falloff rates between 1.6 and 2, and that the proportion of high-frequency radiation decays as the rupture grows. During this period, however, the overall radiated energy rate is weak at all azimuths (Figure 5d). Around 20 s, backprojection and finite-fault inversion results [*Fan and Shearer*, 2015; *Yagi and Okuwaki*, 2015] show that the rupture may be located on a lateral ramp, the Trisuli Transform [*Berger et al.*, 2004; *Mugnier et al.*, 2011], and the radiated energy rate peaks. The high-frequency falloff rate stabilizes at $n = 2$, and the energy portion carried by intermediate frequencies (0.2 Hz–0.5 Hz) maintains a steady value of 60%. Between azimuths of 130° and 250°, we see two distinct high-energy pulses, also imaged by the *Fan and Shearer* [2015] backprojection to be almost collocated with the Trisuli Transform. *Adda-Bedia and Madariaga* [2008] predict that antiplane shear ruptures (mode III) that propagate through kinks can emit stopping phases at the kink (of ω^{-2} high-frequency decay) and can produce less radiation after passage through the kink. A plausible interpretation of the two successive decreases in radiated energy rate at 20 and 25 s is that they are related to the sharpness of the lateral ramp. After 25 s, we see a clear decrease of radiated energy rate, although the backprojection results locate the rupture to be where most of the moment is released (i.e., the GCMT location and geodetic slip inversions) [*Lindsey et al.*, 2015]. *Fan and Shearer* [2015]'s results also infer a loss in high-frequency coherence compared to the low-frequency coherence. At this location and compared to the onset of the rupture, the large moment release and the lack of emission of high frequencies support the hypothesis of a relatively low stress drop underneath Kathmandu.

From 35–40 s, where *P* amplitudes start to decrease, our seismograms are increasingly contaminated by the stronger *sP* phase, and we do not pursue a time-varying analysis of the radiated energy rate.

4. Conclusions

Spectral analysis of the 2015 Nepal earthquake sequence allows us to probe the structure of the MHT and explore dynamical effects predicted by fracture mechanics. Although contaminated by depth phases, we can accurately estimate the source parameters of the *P* wave train by correcting for the effects of destructive interference. Our approach assumes a point source and is most efficient for rather smooth source time function but likely loses effectiveness as the moment-rate function becomes complex. We find that the *M*7.8 and *M*7.3 events have stress drops that are typical for the region [*Allmann and Shearer*, 2009] but that the *M*6.8 has a larger stress drop. We propose that dynamic weakening mechanisms control the runaway rupture style of the onset of the *M*7.8 main shock and of the *M*6.8 aftershock, as suggested by the correlations in the shape of their waveforms. The region of large main shock moment release, inferred from long-period surface waves (GCMT) and geodesy, generates relatively little high-frequency energy and thus seems to occur on either a smoother or more lubricated part of the MHT. The *M*7.8 main shock sits at the boundary of two large historical M8+ Himalayan great earthquakes and provides new constraints on rupture propagation through geometrical barriers.

Acknowledgments

The authors thank Simon Klemperer and Brad Lipovsky for helpful discussions. The Global Seismographic Network (GSN) is a cooperative scientific facility operated jointly by the Incorporated Research Institutions for Seismology (IRIS), the United States Geological Survey (USGS), and the National Science Foundation (NSF), under cooperative agreement EAR-1261681. The data are available at the IRIS Data Management Center. The maps were generated using Generic Mapping Tools [*Wessel and Smith*, 1998]. This work is supported partially by a Green Postdoctoral Fellowship at IGPP/UCSD and by NSF grant EAR 111111.

The Editor thanks Jean-Philippe Avouac and an anonymous reviewer for their assistance in evaluating this paper.

References

Abercrombie, R. E. (2014), Stress drops of repeating earthquakes on the San Andreas Fault at Parkfield, *Geophys. Res. Lett.*, *41*, 8784–8791, doi:10.1002/2014GL062079.

Adda-Bedia, M., and R. Madariaga (2008), Seismic radiation from a kink on an antiplane fault, *Bull. Seismol. Soc. Am.*, *98*(5), 2291–2302.

Ader, T., et al. (2012), Convergence rate across the Nepal Himalaya and interseismic coupling on the Main Himalayan Thrust: Implications for seismic hazard, *J. Geophys. Res.*, *117*, B04403, doi:10.1029/2011JB009071.

Allmann, B. P., and P. M. Shearer (2009), Global variations of stress drop for moderate to large earthquakes, *J. Geophys. Res.*, *114*, B01310, doi:10.1029/2008JB005821.

Ambraseys, N. N., and J. Douglas (2004), Magnitude calibration of north Indian earthquakes, *Geophys. J. Int.*, *159*, 165–206.

Avouac, J.-P., L. Meng, S. Wei, T. Wang, and J.-P. Ampuero (2015), Lower edge of locked main Himalayan thrust unzipped by the 2015 Gorkha earthquake, *Nat. Geosci.*, *8*, 708–711.

Baltay, A. A., G. A. Prieto, and G. C. Beroza (2010), Radiated seismic energy from coda measurements and no scaling in apparent stress with seismic moment, *J. Geophys. Res.*, *115*, B08314, doi:10.1029/2009JB006736.

Baltay, A. A., G. C. Beroza, and S. Ide (2014), Radiated energy of great earthquakes from teleseismic empirical Green's function deconvolution, *Pure Appl. Geophys.*, *171*(10), 2841–2862.

Berger, A., F. Jouanne, R. Hassani, and J. L. Mugnier (2004), Modelling the spatial distribution of present-day deformation in Nepal: How cylindrical is the Main Himalayan Thrust in Nepal?, *Geophys. J. Int.*, *156*, 94–114.

Beroza, G. C., and W. L. Ellsworth (1996), Properties of the seismic nucleation phase, *Tectonophysics*, *261*, 209–227.

Bilham, R. (1995), Location and magnitude of the 1833 Nepal earthquake and its relation to the rupture zones of contiguous great Himalayan earthquakes, *Curr. Sci.*, *69*(2), 101–128.

Bilham, R., K. Larson, J. Freymueller, and Project Idylhim Members (1997), GPS measurements of present-day convergence across the Nepal Himalaya, *Nature*, *386*, 61–63.

Boatwright, J. (1980), A spectral theory for circular seismic sources; simple estimates of source dimension, dynamic stress drop, and radiated energy, *Bull. Seismol. Soc. Am.*, *70*(1), 1–27.

Bollinger, L., F. Perrier, J. P. Avouac, S. Sapkota, U. Gautam, and D. R. Tiwari (2007), Seasonal modulation of seismicity in the Himalaya of Nepal, *Geophys. Res. Lett.*, *34*, L08304, doi:10.1029/2006GL029192.

Cattin, R., and J. P. Avouac (2000), Modeling mountain building and the seismic cycle in the Himalaya of Nepal, *J. Geophys. Res.*, *105*(B6), 13,389–13,407.

Choy, G. L., and J. L. Boatwright (1995), Global patterns of radiated seismic energy and apparent stress, *J. Geophys. Res.*, *200*, 18,205–18,228.

Convers, J. A., and A. V. Newman (2011), Global evaluation of large earthquakes energy from 1997 through mid-2010, *J. Geophys. Res.*, *116*, B08304, doi:10.1029/2010JB007928.

Engdahl, E. R., R. D. van der Hilst, and R. Buland (1998), Global teleseismic earthquake relocation with improved travel times and procedures for depth determination, *Bull. Seismol. Soc. Am.*, *88*(3), 722–743.

Fan, W., and P. M. Shearer (2015), Detailed rupture imaging of the 25 April 2015 Nepal earthquake using teleseismic P waves, *Geophys. Res. Lett.*, *42*(14), 5744–5752, doi:10.1002/2015GL064587.

Galetzka, J., et al. (2015), Slip pulse and resonance of Kathmandu basin during the 2015 Mw 7.8 Gorkha earthquake, Nepal imaged with Geodesy, *Science*, *349*(6252), 1091–1095, doi:10.1126/science.aac6383.

Hanks, T. C. (1981), The corner frequency shift, earthquake source models, and *Q*, *Bull. Seismol. Soc. Am.*, *71*(3), 597–612.

Houston, H. (2001), Influence of depth, focal mechanism, and tectonic setting on the shape and duration of earthquake source time functions, *J. Geophys. Res.*, *106*(B6), 11,137–11,150.

Jumar, S., S. G. Wesnousky, T. K. Rockwell, R. W. Briggs, V. C. Thakur, and R. Jayangondaperumal (2006), Paleoseismic evident of great surface rupture earthquakes along the Indian Himalaya, *J. Geophys. Res.*, *111*, B03304, doi:10.1029/2004JB003309.

Kaneko, Y., and P. M. Shearer (2014), Seismic source spectra and estimated stress drop from cohesive-zone models of circular subshear rupture, *Geophys. J. Int.*, *197*, 1002–1015.

Kaneko, Y., and P. M. Shearer (2015), Variability of seismic source spectra, estimated stress drop and radiated energy, derived from cohesive-zone models of symmetrical and asymmetrical circular and elliptical ruptures, *J. Geophys. Res. Solid Earth*, *120*, 1053–1079, doi:10.1002/2014JB011642.

Kostrov, B. (1974), Self-similar problems of propagation of shear cracks, *J. Appl. Maths Mech.*, *28*, 1977–1087.
Langston, C. A. (1978), Moment, corner frequencies, and the free surface, *J. Geophys. Res.*, *83*(B7), 3422–3426.
Langston, C. A. (1982), Comments on "The corner frequency shift, earthquake source models, and Q" by T. C. Hanks, *Bull. Seismol. Soc. Am.*, *72*(4), 1427–1432.
Lavé, J., and J. P. Avouac (2001), Fluvial incision and tectonic uplift across the Himalayas of central Nepal, *J. Geophys. Res.*, *106*(B11), 26,651–26,591.
Lemonnier, C., G. Marquis, F. Perrier, J. P. Avouac, G. Chitrakar, B. Kafle, S. Sapkota, U. Gautam, D. Tiwari, and M. Bano (1999), Electrical structure of the Himalaya of Central Nepal: High conductivity around the mid-crustal ramp along the MHT, *Geophys. Res. Lett.*, *26*(21), 3261–3264.
Lindsey, E. O., R. Natsuaki, X. Xu, M. Shimada, M. Hashimoto, D. Melgar, and D. T. Sandwell (2015), Line of sight displacement from the ALOS-2 interferometry: M_w 7.8 Gorkha earthquake and M_w 7.3 aftershock, *Geophys. Res. Lett.*, *42*, 6655–6622, doi:10.1002/2015GL065385.
Madariaga, R. (1976), Dynamics of an expanding circular fault, *Bull. Seismol. Soc. Am.*, *66*(3), 639–666.
Mayeda, K., and W. R. Walter (1996), Moment, energy, stress drop, and source spectra of western United States earthquakes from regional coda envelopes, *J. Geophys. Res.*, *101*(B5), 11,195–11,208.
Mugnier, J. L., P. Huyghe, A. P. Gajurel, B. N. Upreti, and F. Jouanne (2011), Seismites in the Kathmandu basin and seismic hazard in central Himalaya, *Tectonophysics*, *509*, 33–49.
Mugnier, J. L., A. Gajurel, P. Huyghe, R. Jayangondaperumal, F. Jouanne, and B. Upreti (2013), Structural interpretation of the great earthquakes in the last millennium in the central Himalaya, *Earth Sci. Rev.*, *127*, 30–47.
Pandey, M. R., R. P. Tandukar, J. P. Avouac, J. Vergne, and T. Héritier (1999), Seismotectonics of the Nepal Himalaya from a local seismic network, *J. Asian Earth Sci.*, *17*, 703–712.
Robert, X., P. van der Beek, J. Braun, C. Perry, and J.-L. Mugnier (2011), Control of detachment geometry on lateral variations in exhumation rates in the Himalaya: Insights from low-temperature thermochronology and numerical modeling, *J. Geophys. Res.*, *116*, B05202, doi:10.1029/2010JB007893.
Robinson, D. M., P. G. DeCelles, P. J. Patchett, and C. N. Garzione (2001), The kinematic evolution of the Nepalese Himalayas of western Nepal, *Earth Planet. Sci. Lett.*, *192*, 507–521.
Shi, Z., and Y. Ben-Zion (2006), Dynamic rupture on a bimaterial interface governed by slip-weakening friction, *Geophys. J. Int.*, *165*(2), 469–484.
Warren, L. M., and P. M. Shearer (2005), Using the effects of depth pPhases on P-wave spectra to determine earthquake depths, *Bull. Seismol. Soc. Am.*, *95*(1), 173–184.
Wessel, P., and H. F. Smith (1998), New, improved version of generic mapping tools released, *Eos Trans. AGU*, *79*(47), 579, doi:10.1029/98EO00426.
Yagi, Y., and R. Okuwaki (2015), Integrated seismic source model of the 2015 Gorkha, Nepal, earthquake, *Geophys. Res. Lett.*, *42*, 6229–6235, doi:10.1002/2015GL064995.